

Article

Incompressible Smoothed Particle Hydrodynamics Simulation of Sediment Erosion around Submarine Pipelines

Sheng Yan ¹, Dong Wang ^{1,2,3,4,*}, Yan Li ^{2,*}, Yu Gao ³, Jianguo Lin ³ and Yawei Shi ³

¹ School of Transportation Engineering, Dalian Maritime University, Dalian 116026, China; yansheng20210039@dlnu.edu.cn

² Fujian Province Key Laboratory of Ship and Ocean Engineering, Xiamen 361005, China

³ School of Environmental Science and Engineering, Dalian Maritime University, Dalian 116026, China; gaoyu2424@163.com (Y.G.); ljglin@dlnu.edu.cn (J.L.); ywshi@dlnu.edu.cn (Y.S.)

⁴ State Key Laboratory of Hydraulic Engineering Intelligent Construction and Operation, Tianjin University, Tianjin 300072, China

* Correspondence: wang_dong@dlnu.edu.cn (D.W.); liyan1987me@jmu.edu.cn (Y.L.)

Abstract: Sediment erosion around submarine pipelines is a popular topic, widely investigated in both ocean and submarine-pipeline engineering. In this paper, the incompressible smoothed-particle hydrodynamics (ISPH) method is modified for simulation of local scouring process around the submarine pipeline under the action of unidirectional flow. The erosion model is based on the Clear Water Particle–Turbid Water Particle–Critical Shear Stress (CWP–TWP–CSS) concept, and a sand–water two-phase model is proposed to deal with the sediment-entrained flow. The results of the numerical simulation are compared with the experimental data to verify the accuracy and applicability of the numerical model. The scouring process around the pipeline is investigated under different conditions, i.e., pipeline diameters, gap ratios, and flow velocities. The ISPH model is further used to study the flow characteristics of the scour pits around the submarine pipeline and the influence of the vortices on the maximum scour depth, to provide a theoretical basis for the stability design of submarine pipelines.

Keywords: submarine pipeline; ISPH; sediment erosion model; shear stress



Citation: Yan, S.; Wang, D.; Li, Y.; Gao, Y.; Lin, J.; Shi, Y. Incompressible Smoothed Particle Hydrodynamics Simulation of Sediment Erosion around Submarine Pipelines. *Water* **2024**, *16*, 1445. <https://doi.org/10.3390/w16101445>

Academic Editor: Roberto Gaudio

Received: 14 April 2024

Revised: 13 May 2024

Accepted: 15 May 2024

Published: 18 May 2024



Copyright: © 2024 by the authors. Licensee MDPI, Basel, Switzerland. This article is an open access article distributed under the terms and conditions of the Creative Commons Attribution (CC BY) license (<https://creativecommons.org/licenses/by/4.0/>).

1. Introduction

In recent years, there has been an increased utilization of offshore petroleum resources globally, leading to rapid developments in offshore engineering technologies such as offshore oil drilling platforms and submarine oil pipelines. Among these, submarine oil pipelines play a crucial role as the primary means of transporting marine oil and gas resources. However, the installation of submarine oil pipelines on the seabed and their frequent burial in sediment pose significant challenges for their inspection and maintenance. The corrosive nature of seawater, damage caused by third-party activities, and the complex and ever-changing marine environment all present serious challenges to the safety and stability of submarine oil pipelines. In the event of an accident, not only would there be substantial economic losses, but also potential pollution of the marine environment.

Erosion of the sediment around submarine pipelines is a common issue in engineering, as excessive erosion can lead directly to pipeline damage. Consequently, this issue has received significant attention from engineering designers and has remained a popular research topic in the academic community [1–5]. To assess the safety of submarine pipelines placed on the seabed, accurate prediction of the surrounding sediment-erosion process and scour depth is essential [2]. In recent years, with the rapid development of computer technology, numerical simulation studies have gained widespread attention due to their low investment cost, adaptability to various fluid and complex boundaries, high flexibility, and absence of scale effects. Given the difficulties in directly measuring the specific local

scouring processes around hydraulic and marine structures, economical and efficient numerical simulations have become a more effective approach [6].

Regarding the study of sediment scour mechanisms at the bottom of pipelines under unidirectional flow conditions, Chiew [1] explored the principles behind scour phenomena on non-cohesive seabeds, and proposed methods to prevent scour near pipelines, considering pipelines as the main cause of scour. Chiew [2] further developed an empirical function to predict the maximum scour depth of submarine pipelines under specific conditions. The research conducted by Dey and Singh [7] suggested that the equilibrium scour depth increases with increasing water flow depth. Cheng et al. [8] investigated the propagation velocity of three-dimensional scour after the initiation of scour around submarine pipelines under steady flow conditions and proposed a prediction formula. In the study of scour development around submarine pipelines, experimental research by Sumer et al. [9] indicated that scour always occurs locally and develops along the direction of the pipeline. Sumer et al. [10] demonstrated that scour downstream of the pipeline is significantly influenced by organized wake flow, which involves the shedding and downstream stable flow of large-scale vortices from the pipeline.

In numerical simulation studies of pipelines under unidirectional flow, Li et al. [11] proposed a numerical model based on potential flow theory to simulate the formation of equilibrium scour holes beneath submarine pipelines, allowing for approximate estimation of scour depth under clear water conditions. Liang et al. [12] developed a two-dimensional numerical model for flow conditions and examined the simulation performance of two turbulence models, the standard k - ϵ model and the subgrid-scale (SGS) model, for relevant scour processes. Liang et al. [13] studied the Reynolds number dependency of two-dimensional scour beneath submarine pipelines in steady flow using a numerical model and the difference in scour developments beneath a model pipeline and the corresponding prototype pipeline. Zhao and Cheng [14] utilized numerical methods to investigate localized scour beneath a backfill pipeline under steady flow conditions. The research revealed that gap ratio significantly affects the flow and scour profiles. Yeganeh-Bakhtiary et al. [15] developed a Euler–Euler two-phase model to study tunnel erosion beneath submarine pipelines exposed to unidirectional flow. The transport rate beneath the pipeline rapidly increases during the initial stage and gradually decreases as tunnel erosion beneath the pipeline concludes.

The Smoothed-Particle Hydrodynamics (SPH) method has been widely applied in computational fluid dynamics, particularly in simulating transient and non-steady flows involving complex interface surfaces [16]. However, there has been relatively limited research on sediment initiation and erosion under turbulent conditions [17–19]. Wang et al. [17] modified the incompressible SPH method to simulate the erosion process behind the seawall under continuous tsunami overflow. Fonty et al. [18] employed an SPH formulation to solve two-phase flow with high density ratios. Bertevas et al. [19] showed a two-phase mixture model in SPH formulation and its application to turbulent sediment transport. The disturbance caused by submarine pipelines to the flow field results in complex variations in both horizontal- and vertical-flow patterns [20], which has an important effect on sediment transport. Due to the lack of detailed validation for turbulence and sediment transport models in particle methods, the suitability of SPH for simulating localized sediment scour and deposition around pipelines has not been fully understood [21–23]. Mirmohammadi and Ketabdari [21] presented an SPH approach to simulate scouring due to waves around a marine pipeline on a sloping sea bed, in which sediment particles were modeled as non-Newtonian fluid and the Bingham model was utilized for simulation of the seabed behavior. Morteza et al. [22] used the similar SPH two-phase flow model to simulate current-induced scour beneath marine pipelines. Wang et al. [23] proposed a three-dimensional ISPH erosion model to simulate the scouring process around large vertical cylinders, which exhibited good agreement with experimental measurements in terms of scour morphology and range.

The main work of this article is to numerically simulate the erosion of sediment around submarine pipelines using the ISPH method. The work is presented as follows. Following the Introduction, the ISPH method is presented. It couples a two-phase flow model, an SPS (sub-particle-scale) turbulence model, and the developed clear water particle–turbid water particle–critical shear stress (CWP-TWP-CSS) sediment initiation and erosion model [17] to simulate local scour around a submarine pipeline under the action of two-dimensional unidirectional water flow. Then, validation of the model against the measurement is given, together with comparison with previous models. Both a fixed-bed flow field and moving-bed scour model are established, and the numerical simulation results are compared with the scour pit morphology and cross-sectional flow velocities from experimental data in the literature to validate the accuracy and applicability of the numerical model in this study. Next, a numerical flume is established for two-dimensional unidirectional-flow scour modeling, and studies on sediment erosion around the pipeline are conducted under different conditions, including different pipeline diameters, gap ratios, and inlet flow velocities. The numerical simulation results are discussed and analyzed to study the influence of different conditions on the depth of pipeline scour and the development process of scouring. Next, discussions follow about potential limitations of the model and recommendations for future research. Finally, the research conclusions are drawn.

2. Method

The ISPH method discretizes the fluid in the computational domain into discrete particles of the same size. Each particle has its own physical quantities such as density, mass, velocity, etc., and numerical calculations are performed based on the Navier–Stokes (N-S) equations.

2.1. The Spatially Averaged N-S Equation

Governing equations include the mass conservation equation and the incompressible form of the N-S equation in the Lagrangian frame with the operation of spatial filter, closed by the SPS (sub-particle-scale) turbulence model [24], which is equivalent to the LES in the Eulerian frame.

$$\nabla \cdot \mathbf{u} = 0, \quad (1)$$

$$\frac{D\mathbf{u}}{Dt} = -\frac{1}{\rho_0} \nabla p + \mathbf{g} + \nu_0 \nabla^2 \mathbf{u} + \frac{1}{\rho_0} \nabla \cdot \vec{\boldsymbol{\tau}}, \quad (2)$$

where D/Dt denotes the total derivative, \mathbf{u} represents the spatially filtered velocity, ρ_0 represents the density of fluid, ν_0 represents the molecular viscosity, \mathbf{g} denotes the gravitational acceleration, p is the pressure and $\vec{\boldsymbol{\tau}}$ represents the SPS stress tensor, which can be calculated by the Boussinesq eddy-viscosity assumption,

$$\frac{\vec{\boldsymbol{\tau}}}{\rho_0} = 2\nu_t \vec{\boldsymbol{S}} - \frac{2}{3}k \vec{\boldsymbol{I}}, \quad (3)$$

where $\vec{\boldsymbol{S}}$ denotes the strain rate tensor of the filtered velocity, k represents the SPS turbulent kinetic energy, $\vec{\boldsymbol{I}}$ denotes the identical matrix in the tensor form, and ν_t denotes the turbulent eddy viscosity and can be evaluated by the Smagorinsky sub-grid scale model [25]. The detailed information for the SPS stress model can be found in Wang et al. [16].

2.2. Numerical Algorithms

The two-step projection approach is used to solve Equations (1) and (2). Following Chorin and Marsden [26], the algorithm is expressed as follows,

$$\mathbf{u}^{n+1} = \mathbf{u}^n + \Delta \mathbf{u}^* + \Delta \mathbf{u}^{**}, \quad (4)$$

$$\Delta \mathbf{u}^* = (g + \nu_0 \nabla^2 \mathbf{u}^n + \frac{1}{\rho_0} \nabla \cdot \vec{\tau}^n) \Delta t, \tag{5}$$

$$\Delta \mathbf{u}^{**} = -\frac{1}{\rho_0} \nabla p^{n+1} \Delta t, \tag{6}$$

where \mathbf{u}^n and \mathbf{u}^{n+1} represent the flow velocity at time levels n and $n + 1$, respectively; Δt is the time step; $\Delta \mathbf{u}^*$ denotes the increment of velocity in the prediction step; the updated position vectors and velocity are $\mathbf{x}^* = \mathbf{x}^n + \mathbf{u}^* \Delta t$ and $\mathbf{u}^* = \mathbf{u}^n + \Delta \mathbf{u}^*$, respectively; and $\Delta \mathbf{u}^{**}$ is the increment of velocity in the correction step.

Substituting $\mathbf{u}^{n+1} = \mathbf{u}^* + \Delta \mathbf{u}^{**}$ into Equation (6) yields

$$\mathbf{u}^{n+1} - \mathbf{u}^* = -\frac{1}{\rho_0} \nabla p^{n+1} \Delta t. \tag{7}$$

Taking the divergence of Equation (7) and considering the continuity requirement $\nabla \cdot \mathbf{u}^{n+1} = 0$ in the next time step, the pressure Poisson equation (PPE) is derived as

$$\frac{\Delta t}{\rho_0} \nabla \cdot (\nabla p^{n+1}) = \nabla \cdot \mathbf{u}^*. \tag{8}$$

The pressure is calculated by solving Equation (8) implicitly. Then, the velocity correction vector at the correction step can be calculated from Equation (6) and the final updated velocity is obtained by Equation (4). Thus, the final updated position vector is $\mathbf{x}^{n+1} = \mathbf{x}^* + \Delta \mathbf{u}^{**} \cdot \Delta t$.

In the ISPH method, the operations for calculating spatial derivatives of physical properties can be written in the following forms:

$$\phi_i^n = \sum_{j=1}^N W_{ij}^n, \tag{9}$$

$$\nabla \cdot \vec{\tau}_i^n = \phi_0 \sum_{j=1}^N \left(\frac{\vec{\tau}_j^n}{\phi_j^{n2}} + \frac{\vec{\tau}_i^n}{\phi_i^{n2}} \right) \cdot \nabla W_{ij}, \tag{10}$$

$$\nu_0 \nabla^2 u_i^n = \nu_0 \phi_0 \sum_{j=1}^N \left(\frac{8}{(\phi_i^n + \phi_j^n)^2} \vec{S}_{j:i}^n \right) \cdot \nabla W_{ij} \tag{11}$$

$$\nabla \cdot (\nabla p_i^{n+1}) = \frac{1}{\phi_0} \sum_{j=1}^N p_{ij}^n \left(\frac{\partial^2 W_{ij}}{\partial (x_{ij}^*)^2} - \frac{1}{x_{ij}^*} \frac{\partial W_{ij}}{\partial x_{ij}^*} \right) \tag{12}$$

where ϕ denotes the particle density and ϕ_0 is the initial particle density at $n = 0$, and $\vec{S}_{j:i}^n$ is the rate of strain for neighboring particles “ j ” with respect to particle “ i ”. The formulation of $\vec{S}_{j:i}^n$ can be found in Khayyer et al. [12]. W is the kernel function employed in ISPH, and calculated by the cubic B-spline function [27]. The Laplacian operator for the pressure field $\nabla \cdot (\nabla p_i^{n+1})$ is discretized by Khayyer and Gotoh [28] by using Equation (12), in which the higher-order Laplacian method has been shown to improve and stabilize the pressure calculation. $p_{ij}^n = p_j^n - p_i^n$ and $\mathbf{x}_{ij}^* = \mathbf{x}_j^* - \mathbf{x}_i^*$ are defined, respectively.

2.3. CWP-TWP-CSS Erosion Model

The CWP-TWP-CSS erosion model is proposed to deal with the process of both bottom erosion and suspended sediment movement within the frame of the ISPH method [16]. Both CWPs and TWPs are proposed to deal with the sediment-entrained flow. The CWPs are the clear water particles originating from the initial setting or inlet boundary, while the TWPs are the turbid water particles of water–sediment mixture originating from bottom erosion.

The initial sediment initiation is determined by comparing the shear force exerted on the wall particles with the critical shear stress (CSS) for sediment initiation. The theoretical zero point for the wall particles is set at the center of a virtual particle located just below the particle about to initiate.

Based on the integral interpolation theory within the ISPH framework, the tangential flow velocity at the target particle is calculated as follows,

$$u_{bi} = \sum_{j \neq i}^M (u(x_j)\cos\theta - v(x_j)\sin\theta)W(|x_j - x_i|, h)V_j, \tag{13}$$

where u_{bi} denotes the tangential flow velocity component of fluid particle i , $u(x_j)$ and $v(x_j)$ are the flow-velocity components of the fluid particles around the target particle, respectively, θ is the slope of the bed, and V_j is the volume of the fluid particles around the target particle.

Similarly, the tangential stress acting on the target particle is solved by the formula of turbulent shear stress [29]

$$\frac{\tau_{bi}}{\rho} = (\kappa s)^2 \left(\frac{du_i}{ds}\right)^2 = (\kappa D_p)^2 \left(\frac{u_{bi}}{D_p}\right)^2, \tag{14}$$

where τ_{bi} denotes the shear stress of fluid particle i , κ denotes the von Kármán constant (0.4), s is the coordinate value of the slope normal, and D_p is the diameter of the numerical model particle.

A critical start-up shear equation for sediment that better characterizes sediment dynamics was proposed by Manenti et al. [30],

$$\tau_{*c} = \frac{\tau_c}{(\gamma_s - \gamma)d} = f\left(\frac{u_{*c}d}{\nu}\right)^2, \tag{15}$$

where τ_{*c} represents the critical Shields number, τ_c is the critical shear stress of sediment, γ_s and γ are the bulk weight of sediment and water, respectively, u_{*c} is the critical drag-flow rate, and d is the particle size of the real sediment in the experiment; f is an implicit function with respect to the particle Reynolds number Re^* , from reviewing the curves in the literature, as in Figure 1.

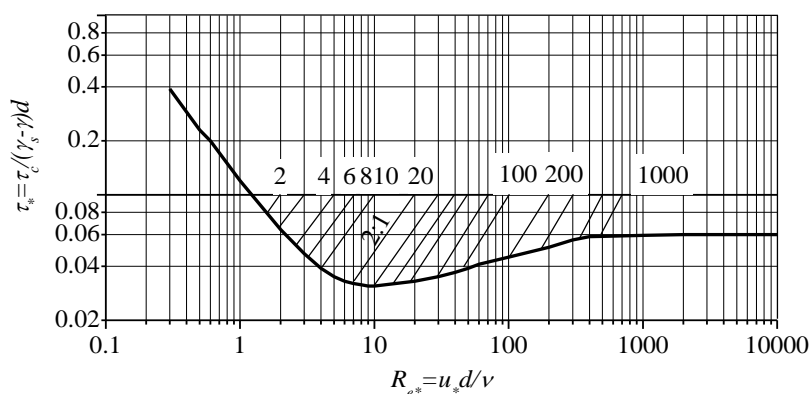


Figure 1. Shields Curve Diagram [31].

If the calculated wall particles are subjected to a shear stress that exceeds the critical starting shear stress of the corrected slope,

$$\tau_{bi} = \tau_{*c}, \tag{16}$$

the particles are transformed from the properties of wall particles to turbid water particles (TWPs) and start from the bottom, recalculating the initial density of the particles and participating in the calculation of the N-S equations to be solved, while the newly exposed virtual particles will become new wall particles. The density of TWPs will be updated in a timely way, according to the method described in Sections 2.1 and 2.2. and the sediment concentration can be obtained from the known values of the densities of the numerical particles.

3. The Validation of the Model

3.1. Validation of the Flow Field

Before simulating the sediment erosion around the submarine pipeline, the flow field calculation around the pipeline is validated using the experimental data from Oner et al. [32]. The model used in the validation has a length of 7.26 m, a total number of particles of 124,259, a numerical particle diameter of 0.005 m, and a pipeline diameter D of 0.05 m. The flow direction is from left to right, with the outflow velocity set to be the same as the inflow velocity, and the water depth is 0.32 m.

Based on the selected measurement points in the experiment, Figure 2 compares the velocity profiles at different distances from the pipeline, namely, $x = -D$, $x = -0.5D$, $x = 0$, $x = 0.5D$, and $x = D$ (the negative sign represents the upstream side of the pipeline). The blue lines represent the numerical results, while the red lines represent the experimental results. It can be observed that the numerical results are in good agreement with the experimental data, confirming that the ISPH numerical model can accurately simulate the flow field changes near the pipeline.

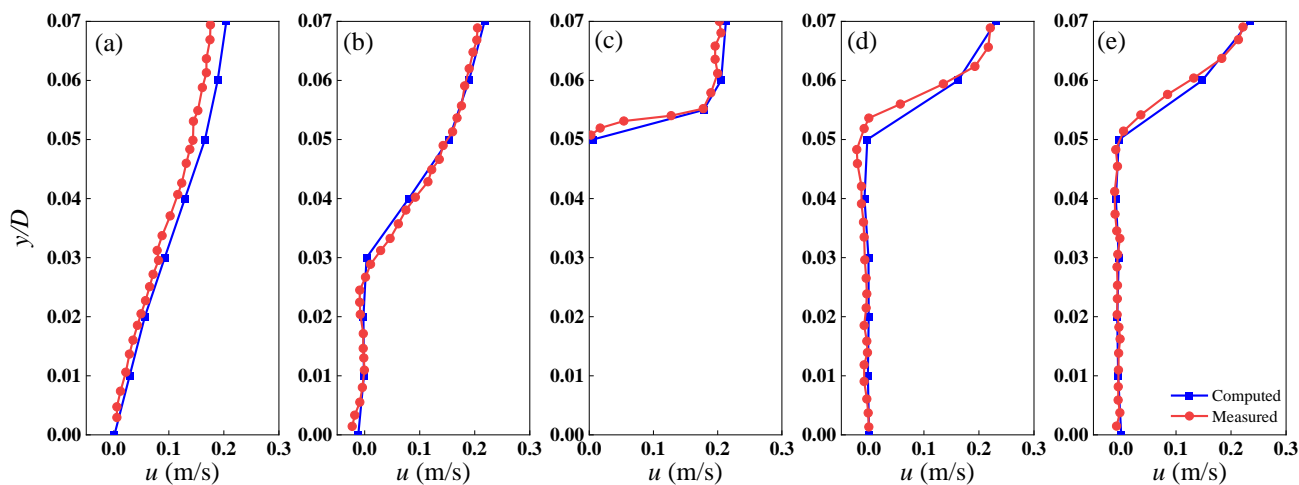


Figure 2. Measured (red line) and computed (blue line) horizontal-velocity profiles at cross-sections $x = -D$ (a), $x = -0.5D$ (b), $x = 0$ (c), $x = 0.5D$ (d), and $x = D$ (e).

To give a quantitative description of the agreement, the following root-mean-square errors are presented in Table 1 for horizontal-velocity profiles at different locations,

$$\epsilon_{mv} = \sqrt{\frac{1}{n} \sum_{i=1}^n (\text{exp}_i - \text{com}_i)^2}, \tag{17}$$

where exp_i and com_i are the experiment and calculation results.

Table 1. The root-mean-square errors for horizontal velocity profiles at different locations.

x	$-D$	$-0.5D$	0	$0.5D$	D
ϵ_{rms} (m/s)	0.0175	0.0083	0.0274	0.0177	0.0090

3.2. Validation of the Sediment Erosion Models

To validate the coupling effect of the turbulence model and sediment erosion model, the scour around a submarine pipeline was simulated. The influence of the gap ratio between the pipeline and the bed on the scour was investigated and compared with the numerical results of Akter-Uz-Zaman [33]. The diameter of the pipeline is set as $D = 0.05$ m, with a total of 126,322 particles and a numerical particle diameter of 0.005 m. It is important to note that particles entering the outflow region are assigned the actual flow velocity at the current time, ensuring a more realistic and stable simulation of the flow field. The inflow velocity is set to 0.65 m/s. Based on the Shields curve and the formula in Figure 1, the estimated critical shear stress for sediment initiation is set to $\tau = 0.1$ N.

Figure 3 shows the velocity contours of the flow field at $t = 3.7$ s, 5.4 s, 7 s, 8.7 s, 10 s, and 11 s, respectively. It can be observed that as scouring progresses, the area below the pipeline is gradually eroded, reaching an equilibrium depth of approximately $0.6 D$. A protruding sand dune appears in the rear, with a height of approximately $0.4 D$ and different slopes on the front and back sides of the sand slope. Figure 3 also demonstrates the impact of the sand slope on the water flow velocity. As the water flow reaches the top of the sand slope, the velocity decreases, leading to sediment deposition. Below the pipeline, the increasing gap causes more sediment particles to be entrained by the flow and carried to the rear of the pipeline, where they interact with the shear flow above the pipeline, generating a wake vortex.

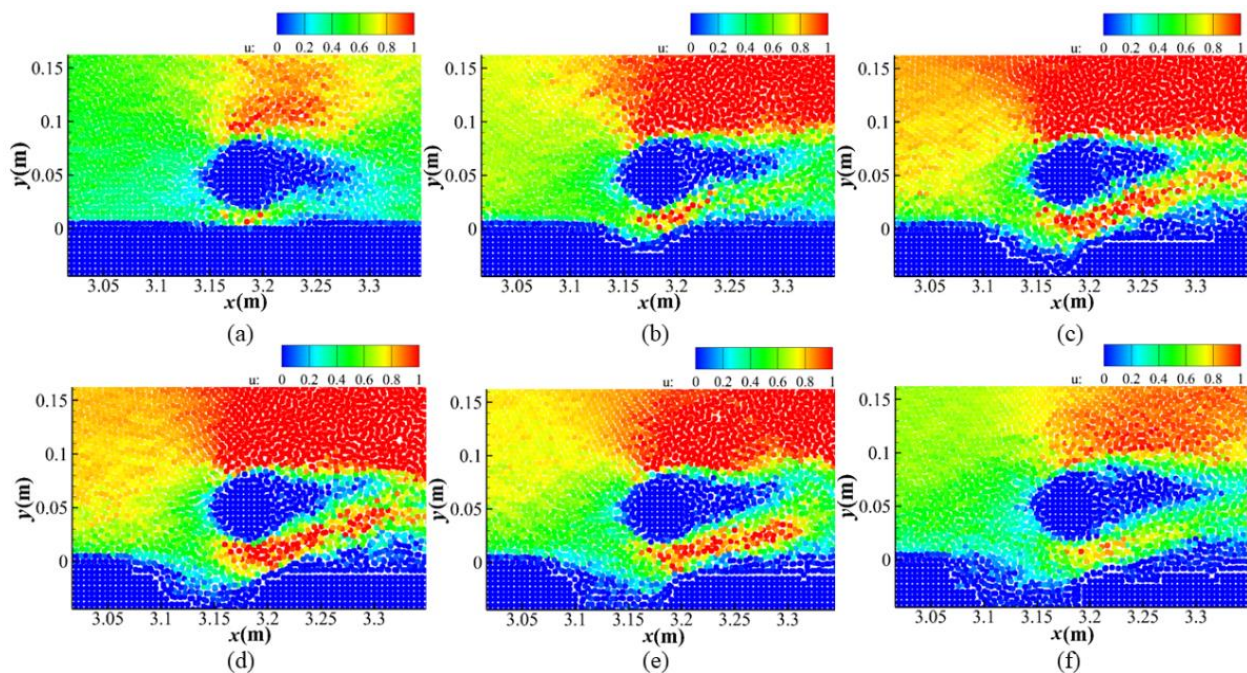


Figure 3. Velocity contours of flow field at $t = 3.7$ s (a), 5.4 s (b), 7 s (c), 8.7 s (d), 10 s (e), and 11 s (f).

To validate the accuracy of the sediment erosion model, four different sets of pipeline gap ratios, e/D , were set in this study, where e represents the distance from the bottom of the pipeline to the bed surface. For example, $e/D = -0.25$ indicates that the pipeline is buried $0.25D$ into the bed. The specific parameters (inlet flow velocity U , pipeline diameter D , water depth h , and gap ratio e/D) are shown in Table 2.

Table 2. Parameters of the scour model.

Test	U (m/s)	D (m)	H (m)	e/D
1	0.65	0.05	0.23	−0.25
2	0.65	0.05	0.23	0.25
3	0.65	0.05	0.23	0.5
4	0.65	0.05	0.23	1.0

In Figure 4, the corresponding gap ratios for (a), (b), (c), and (d) are $e/D = -0.25, 0.25, 0.5,$ and $1.0,$ respectively. By comparing the ISPH simulation results with the SedFoam results of Akter-Uz-Zaman [27], it can be observed that the bed profile results are basically consistent. As the pipeline position increases, the equilibrium scour depth gradually decreases. In the range of $0 < e/D < 1.0,$ it can be found that the bed profiles are greatly influenced by burial depth. In the case of $e/D < 0,$ there is almost no changes for the bed profiles, indicating that the pipeline buried deeper in the sand bed is relatively stable. To give a quantitative description of the agreement, the following root-mean-square errors of simulated bed profiles are presented in Table 3 for four different gap ratios $e/D = -0.25, 0.25, 0.5,$ and $1.0.$

$$\varepsilon_{rms} = \sqrt{\frac{1}{n} \sum_{i=1}^n (\text{ISPH}_i - \text{SedFoam}_i)^2}, \quad (18)$$

where ISPH_i and SedFoam_i are ISPH and SedFoam results.

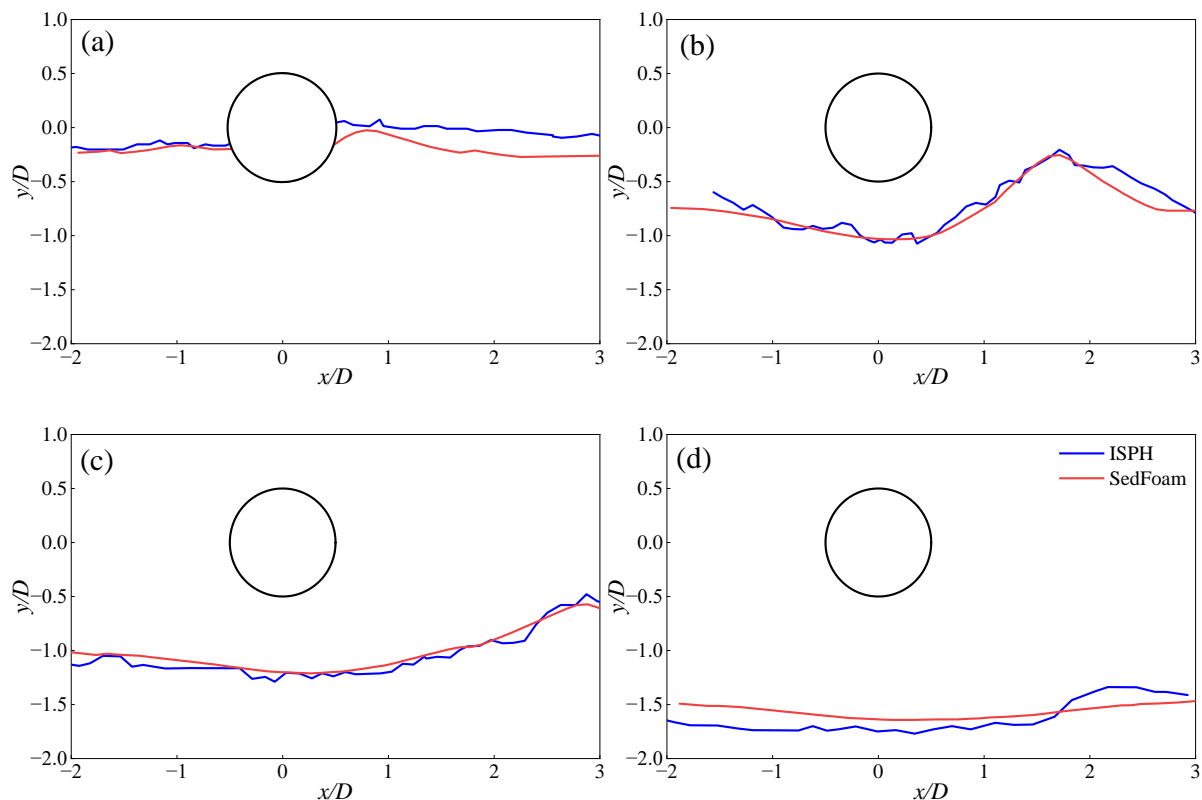


Figure 4. Bed profiles around the pipeline for four different gap ratios $e/D = -0.25$ (a), 0.25 (b), 0.5 (c), and 1.0 (d). Red lines are SedFoam results of Akter-Uz-Zaman [27] and blue lines are ISPH simulation results. The black circle denotes the location of pipeline.

Table 3. The root-mean-square errors of simulated bed profiles for four different gap ratios.

e/D	−0.25	0.25	0.5	1.0
y/D	0.1414	0.0871	0.0565	0.1319

4. ISPH Simulation of Local Scour around Submarine Pipelines

In this section, a numerical flume with dimensions close to actual offshore engineering is established, with a length of 14 m and a sand bed thickness of 0.4 m. The water depth is 2.0 m. The diameter of the pipeline is 0.3 m, and the numerical particle diameter of the model is 0.01 m, with a total of 276,553 particles after discretization. The critical shear stress for sediment initiation is calculated to be $\tau = 0.99$ N, based on the Shields curve and the shear stress calculation formula. In this section, the influence of factors such as the gap ratio e/D between the pipeline and the sediment bed, inflow velocity, and pipeline diameter on the equilibrium scour depth and erosion process will be explored. The specific settings for the calculation conditions are shown in Table 4.

Table 4. Test conditions.

Test	e/D	u_0 (m/s)	D (m)	Re
S1	0	0.65	0.3	1.95×10^5
S2	0	0.8	0.3	2.40×10^5
S3	0	0.95	0.3	2.85×10^5
S4	−0.25	0.95	0.3	2.85×10^5
S5	0.25	0.95	0.3	2.85×10^5
S6	0.5	0.95	0.3	2.85×10^5
S7	0.75	0.95	0.3	2.85×10^5
S8	1	0.95	0.3	2.85×10^5
S9	0	0.95	0.4	3.80×10^5
S10	0	0.95	0.5	4.75×10^5

4.1. Effect of Gap Ratios

The ratio of the distance from the submarine oil pipeline to the sand bed (gap ratio e/D) to the pipeline diameter has a significant impact on the erosion process of sediment around the pipeline. When e/D is less than 1.0, it has a greater impact on the seabed around the pipeline and affects the water flow near the seabed surface.

In order to study the influence of different gap ratios (e/D) on the erosion process and scour depth of the pipeline, this section mainly analyzes the numerical simulation results of the S3, S4, S5, S6, S7, and S8 cases. The scour depth on the seabed around the pipeline increases with time. From Figure 5, it can be observed that at 10 s, when $e/D = -0.25$, sediment starts to mobilize behind the pipeline, transforming into sediment particles and initiating erosion. However, in cases where $e/D \geq 0$, the water flow causes significant erosion on the bottom of the pipeline, leading to rapid erosion development. Moreover, with an increase in the gap ratio e/D , the scour depth also increases. When $e/D = 1.0$, the scour depth at the bottom decreases compared to $e/D = 0.75$, indicating that the influence of the gap ratio on the scour depth diminishes after the pipeline is lifted to a sufficient height.

From Figure 6, it can be observed that at $t = 15$ s, the erosion extent behind the pipeline is greater compared to 10 s for the case of $e/D = -0.25$. In the cases where $e/D \geq 0$, it can be seen that the mobilized sediment accumulates behind the pipeline, forming a sand slope with a noticeable inclination. Similar to 10 s, the scour depth increases with an increase in the gap ratio e/D . When $e/D = 0.5$, the accumulated sand dune behind the pipeline is higher, indicating intense sediment transport around the pipeline. It can be observed that the erosion develops more rapidly in Figure 6 than that in Figure 5. At 15 s, the erosion extent on the sediment bed in front of the pipeline is greater compared to 10 s, and the scour depth also increases. The curve in the x -direction from 5.0 m to 5.2 m shows a significant decrease compared to 10 s.

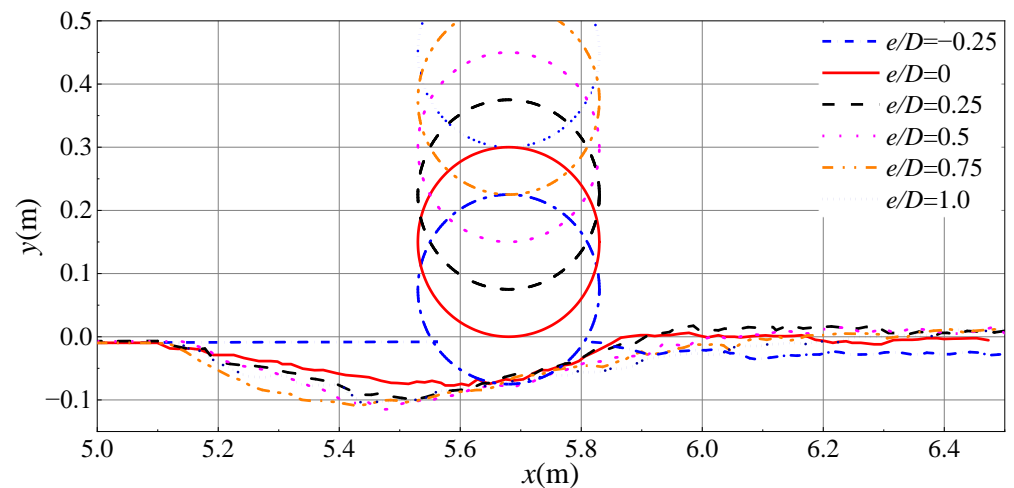


Figure 5. Bed profiles around the pipeline at $t = 10$ s for different gap ratios.

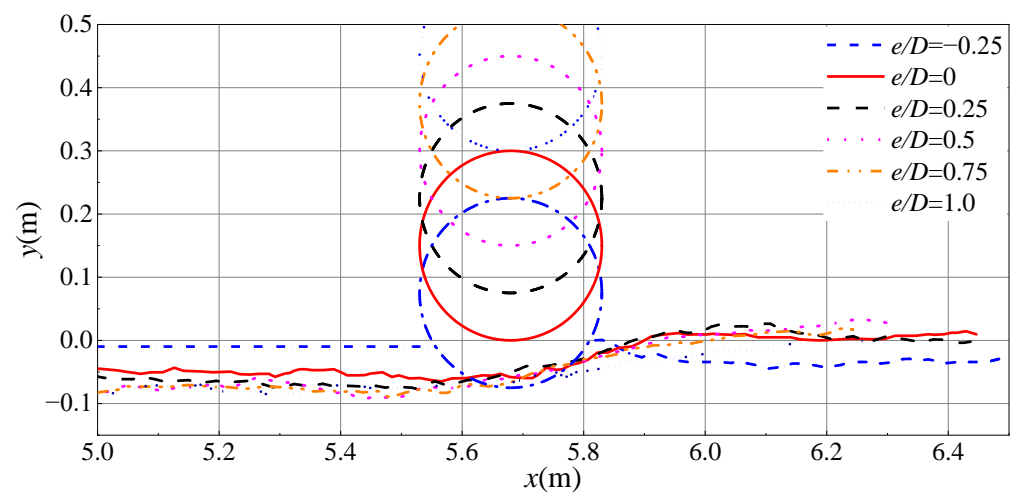


Figure 6. Bed profiles around the pipeline at $t = 15$ s for different gap ratios.

From Figure 7, it can be observed that at 20 s, in the case of $e/D = -0.25$, the erosion extent behind the pipeline increases, and a sand pit forms in front of the pipeline. This is because as erosion progresses, the mobilized sediment in front of the pipeline is carried away by the water flow, forming a sand pit. In the cases where $e/D \geq 0$, the mobilized sediment accumulates behind the pipeline, and a sand pit also forms behind the pipeline. It can be observed that at this point, the surroundings of the pipeline have reached an equilibrium state. The scour depth remains constant. For $e/D = 0.25$, a higher slope sand dune forms behind the pipeline. Additionally, it can be observed that in the case of burial depth $e/D = -0.25$, the erosion development of the pipeline is slower compared to other scenarios, and the scour depth reaches its maximum at this stage.

Figure 8 presents the bed profiles around the pipeline (left column) and velocity contour of the flow field at 10 s for gap ratios $e/D = -0.25, 0$, and 0.25 , respectively. Figure 9 show those for gap ratios $e/D = 0.5, 0.75$, and 1.0 , respectively. The “*pro*” property represents the particle property, with $pro = 10$ representing water particles and $pro = 30$ representing sediment particles (red representing sediment and cylinders, and blue representing water), while “*u*” represents the horizontal flow velocity. The flow direction is from left to right (the same hereinafter).

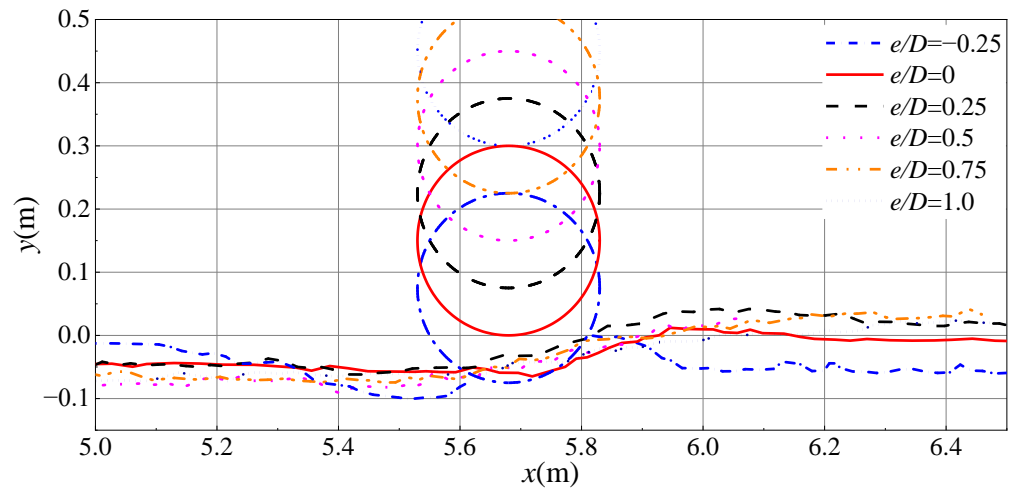


Figure 7. Bed profiles around the pipeline at $t = 20$ s for different gap ratios.

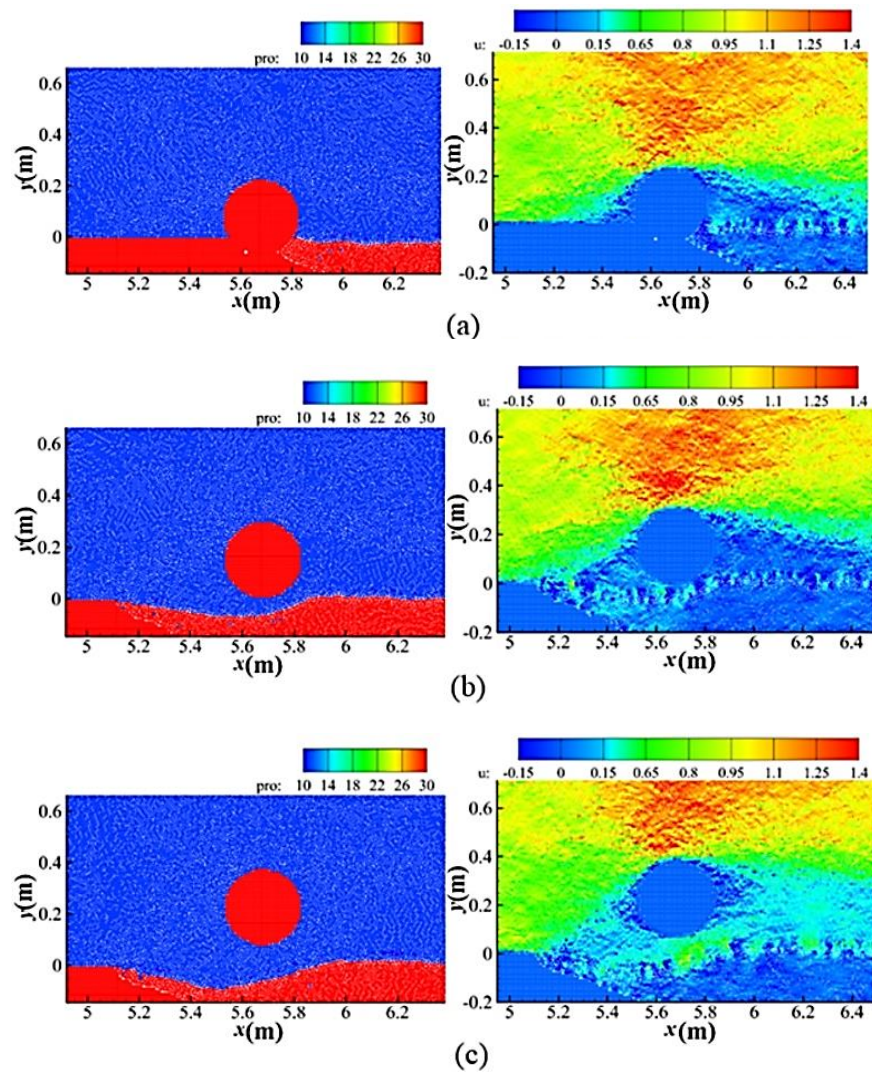


Figure 8. Bed profiles around the pipeline (left column) and velocity contour of the flow field (right column) at 10 s when the gap ratio e/D is -0.25 (a), 0 (b) and 0.25 (c).

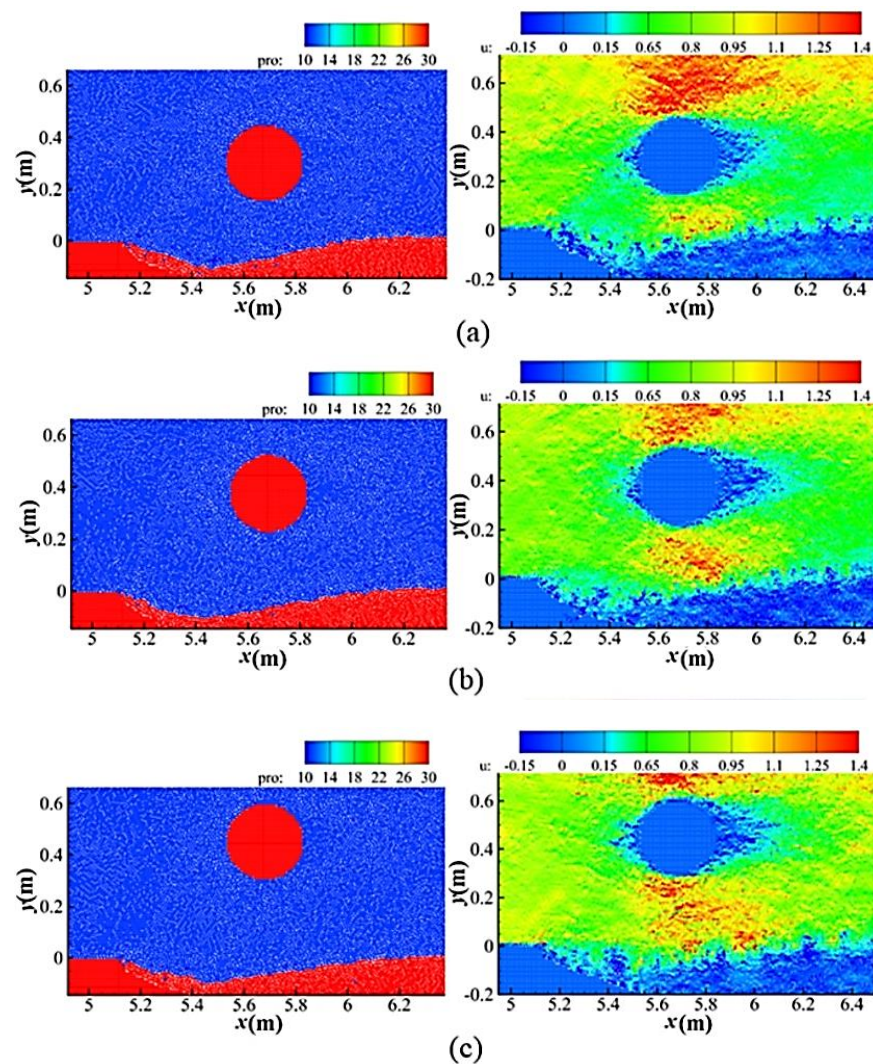


Figure 9. Bed profiles around the pipeline (left column) and velocity contour of the flow field (right column) at 10 s when the gap ratio e/D is 0.5 (a), 0.75 (b) and 1.0 (c).

From Figures 8 and 9, it can be observed that there is a gradual increase in the scour depth below the pipeline as the gap ratio e/D increases. However, when e/D exceeds 0.5, the scour depth below the pipeline no longer undergoes significant changes. Additionally, the sediment accumulation also varies, with sediment accumulation gradually moving away from the pipeline.

To show the influence of different gap ratios (e/D) on the morphology of erosion pits and the maximum scour depth, Figure 10 presents the variation in the maximum scour depth y/D with time for different gap ratios e/D . It can be observed that the erosion intensity develops rapidly during the initial erosion stage, almost several times faster than in the later stage, and follows a certain pattern, where the slope of the curve increases with an increase in the gap ratio. However, as erosion progresses, the change in scour depth tends to reach an equilibrium state, and a larger gap ratio leads to a greater maximum equilibrium scour depth. However, when $e/D = 0.75$ and 1.0, the erosion development near the pipeline is similar, and there is little difference in the scour depth. This is because the gap ratio of the pipeline reaches a certain level, where its influence on the bed erosion is not significant.

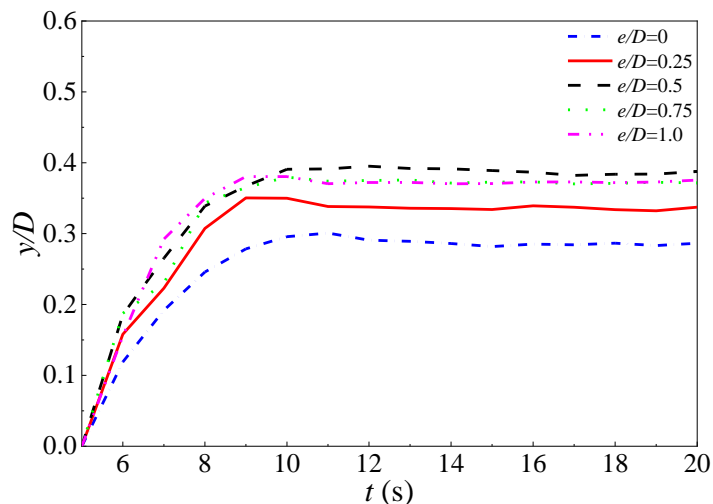


Figure 10. Maximum scour depth over time for different gap ratios.

Figure 11 represents the horizontal velocity profiles near the pipeline at $x = -1.0D$, $x = -0.5D$, $x = 0D$, $x = 0.5D$, and $x = 1.0D$ for gap ratios $e/D = 0, 0.25, 0.5$, and 1.0 , respectively. It can be observed that the flow field develops sufficiently when the flow enters the erosion zone. At $x = -1.0D$, the velocity increases with an increase in the gap ratio. This is due to the flow circulation around the pipeline, which increases the flow velocity above and below the pipeline. At $x = -0.5D$, the flow-velocity variations become more pronounced, due to the influence of the pipeline. At $x = 0D$, it can be visually observed that the velocity increases both above and below the pipeline, due to the obstruction of the pipeline. At $x = 0.5D$, the trend is similar to that in front of the pipeline, but the flow velocity decreases behind the pipeline. At $x = 1.0D$, the flow velocity also decreases, due to the flow circulation around the pipeline. The occurrence of flow separation near the pipeline makes the development of the flow field near the pipeline very complex. Sediment is carried and transported by the water flow, leading to sediment accumulation behind the pipeline and erosion of the bed surface below the pipeline, resulting in an increase in scour depth and an enlargement of vortex size.

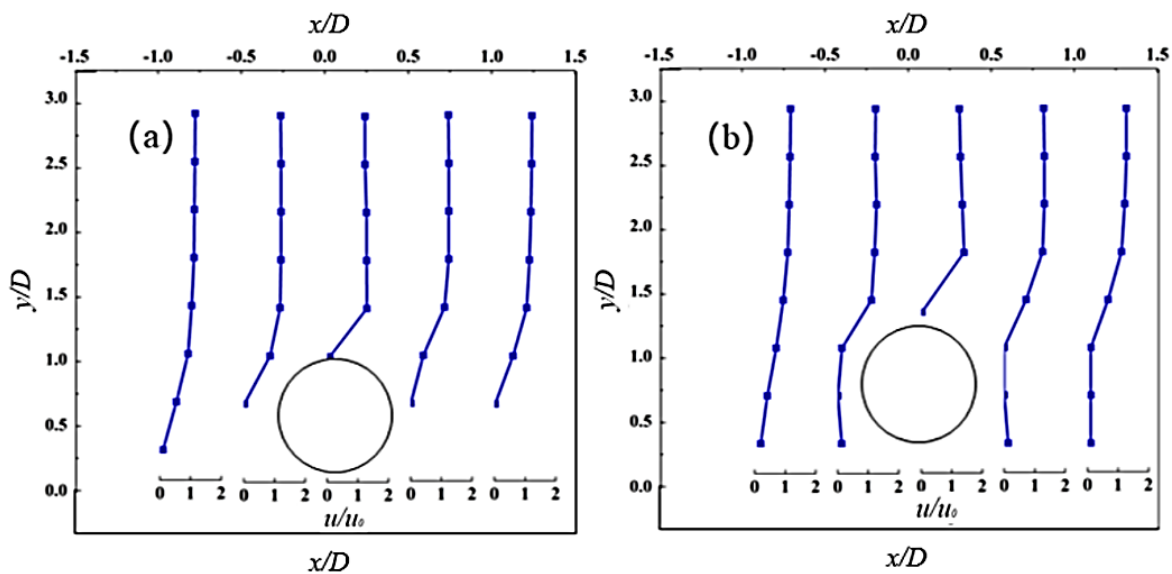


Figure 11. Cont.

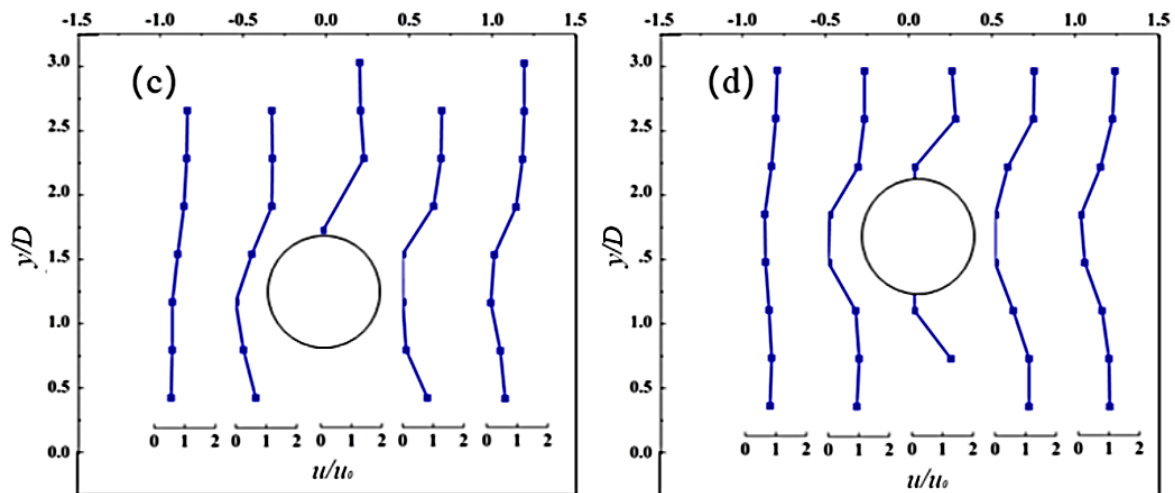


Figure 11. Horizontal velocity profiles around the pipeline for different gap ratios 0 (a), 0.25 (b), 0.5 (c), and 1.0 (d).

4.2. Effect of Different Inlet Flow Velocities

Different inflow velocities have varying impacts on pipeline erosion. In complex underwater environments, the location where the pipeline is laid may be subject to tidal forces, earthquakes, ocean currents, waves, or fishing activities, which can potentially damage the pipeline. However, in deep-sea environments, the impact of waves on submarine pipelines can be negligible. Earthquakes, tsunamis, or human activities such as fishing activities, which may damage submarine pipelines, are occasional events. Therefore, the influence of ocean currents becomes an important factor in causing pipeline scour and has been a major concern for researchers worldwide. In this section, we primarily focus on the study of constant and uniform inflow applied to pipelines laid on the seabed. We aim to explore the impact of different inflow velocities on scour depth, erosion processes, and equilibrium scour time around the pipeline. In this section, we select a pipeline diameter of $D = 0.3$ m, a gap ratio of $e/D = 0$, and three different inflow velocities: 0.65 m/s, 0.8 m/s, and 0.95 m/s. We compare the morphology of erosion pits around the pipeline on the sediment bed and summarize the influence of different inflow velocities on scour depth and the erosion process.

Figures 12–14 show the bed profiles around the pipeline at three instantaneous moments ($t = 10$ s, 15 s, and 20 s) under inlet flow velocities of 0.65 m/s, 0.8 m/s, and 0.95 m/s, respectively. The erosion extent in front of the pipeline at 15 s and 20 s is greater than at 10 s, with larger scour depth. The bed profiles from $x = 5.0$ m to $x = 5.2$ m in the x -direction decrease significantly compared to the bed profiles at 10 s. The erosion pits gradually extend towards the front of the pipeline.

In Figure 15, as the inflow velocity increases from 0.65 m/s to 0.95 m/s, it can be observed that the scour pits below the pipeline gradually become larger. Over time, the scour depth also increases, and there is a significant accumulation of sediment behind the pipeline, with a more pronounced slope. It can be concluded that as the velocity increases, the impact on scour depth becomes greater, showing a proportional relationship. In other words, higher inflow velocities result in deeper scour depths.

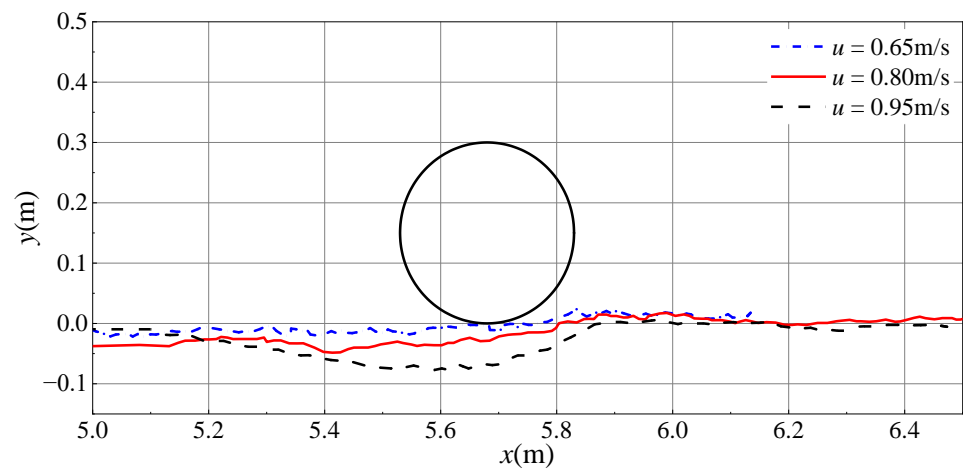


Figure 12. Bed profiles around the pipeline at $t = 10$ s for different inlet flow-velocity conditions. The black circle denotes the location of pipeline.

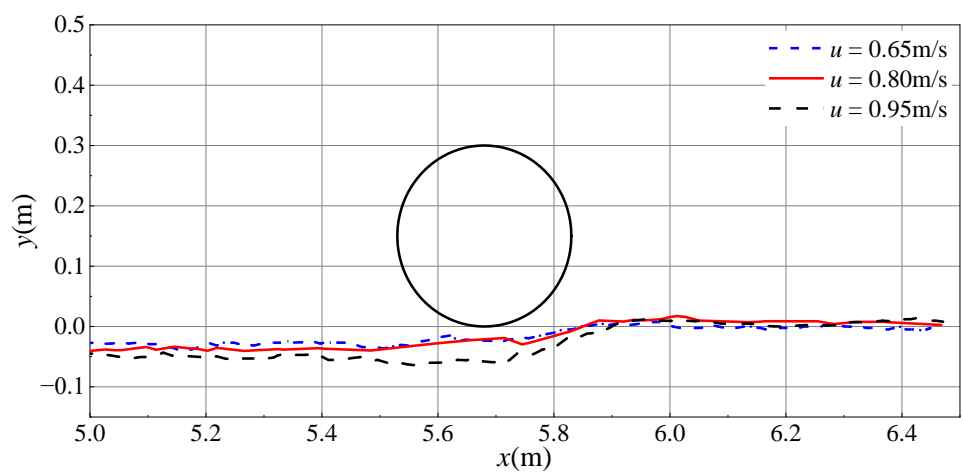


Figure 13. Bed profiles around the pipeline at $t = 15$ s for different inlet inflow-velocity conditions. The black circle denotes the location of pipeline.

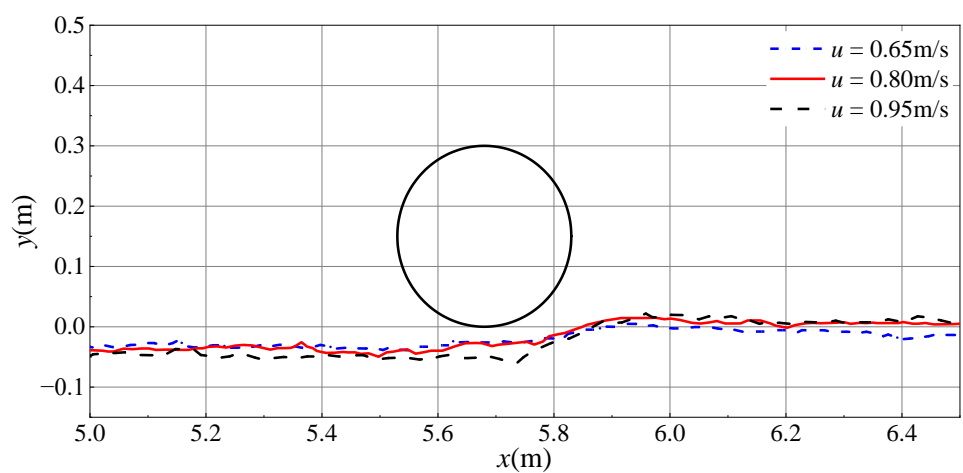


Figure 14. Bed profiles around the pipeline at $t = 20$ s for different inlet flow-velocity conditions. The black circle denotes the location of pipeline.

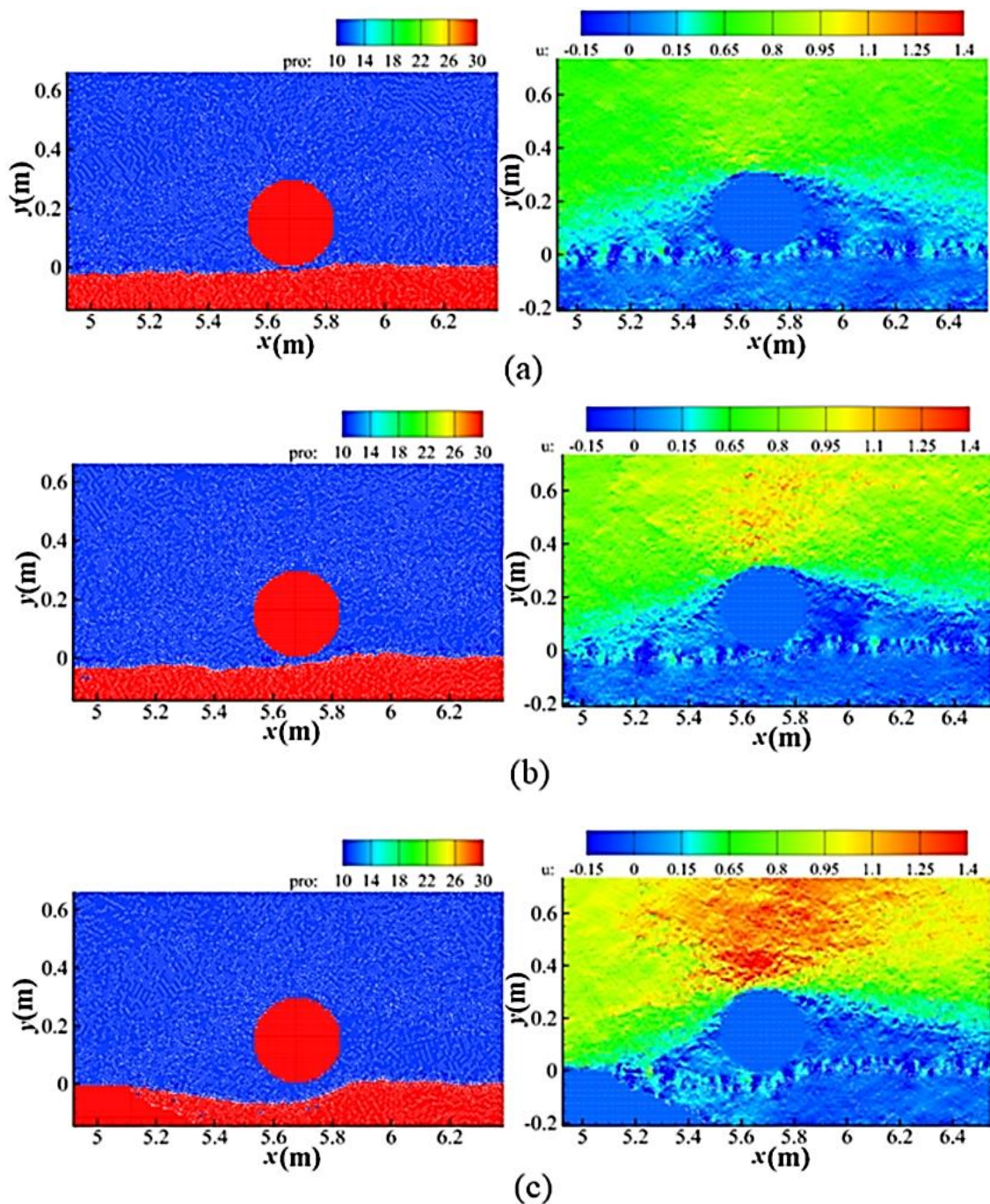


Figure 15. Bed profiles around the pipeline (left column) and velocity contour of the flow field (right column) of incoming flow velocities of 0.65 m/s (a), 0.8 m/s (b) and 0.95 m/s (c).

Figure 16 shows the curve of the maximum scour depth (y/D) as a function of time for different inlet flow velocities. It can be observed that the maximum scour depth increases with time. Under the condition of an inflow velocity of 0.95 m/s, the maximum scour depth near the pipeline can reach $0.3D$. As the inflow velocity increases, the slope of the curve becomes steeper. However, as the erosion progresses, the change in scour depth becomes less significant. A higher inflow velocity results in a larger equilibrium scour depth.

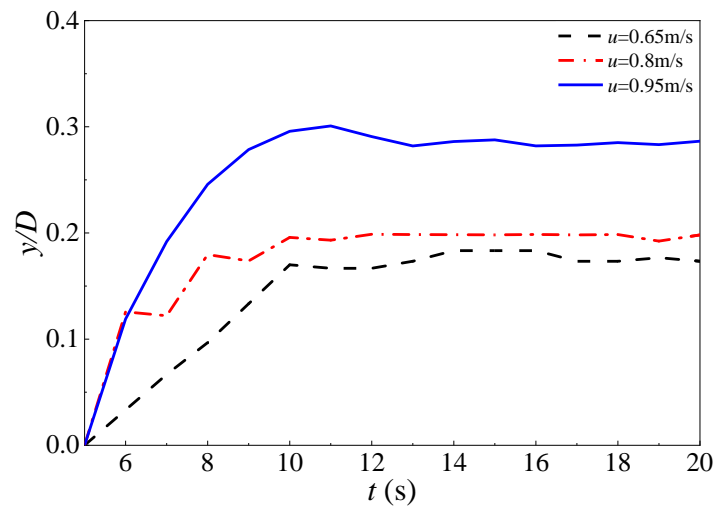


Figure 16. Maximum scour depth over time for different inlet flow velocities.

4.3. Effect of Different Pipeline Diameters

The diameter of submarine pipelines also affects the erosion process around the pipeline. Under the same conditions of water depth, velocity, and burial depth, a larger pipeline diameter results in a more pronounced interaction between the pipeline and the sediment-laden water flow, leading to more significant changes in the flow field velocity. To explore the impact of different pipeline diameters on erosion, we selected a gap ratio of $e/D = 0$ and three different pipeline diameters: $D = 0.3$ m, $D = 0.4$ m, and $D = 0.5$ m, with an inflow velocity of 0.95 m/s. Numerical simulations were conducted to examine the erosion on the bed surface around the pipeline. Figures 17–19 show the morphology of scour pits at 10 s, 15 s, and 20 s, respectively, under conditions of pipeline diameters $D = 0.3$ m, $D = 0.4$ m, and $D = 0.5$ m. When $D = 0.5$ m, the morphology of the scour pits is not significantly different from the other two conditions, but there is a larger accumulation of sediment behind the pipeline. As the pipeline diameter increases, there is a greater accumulation of sediment behind the pipeline, resulting in the formation of higher sand slopes.

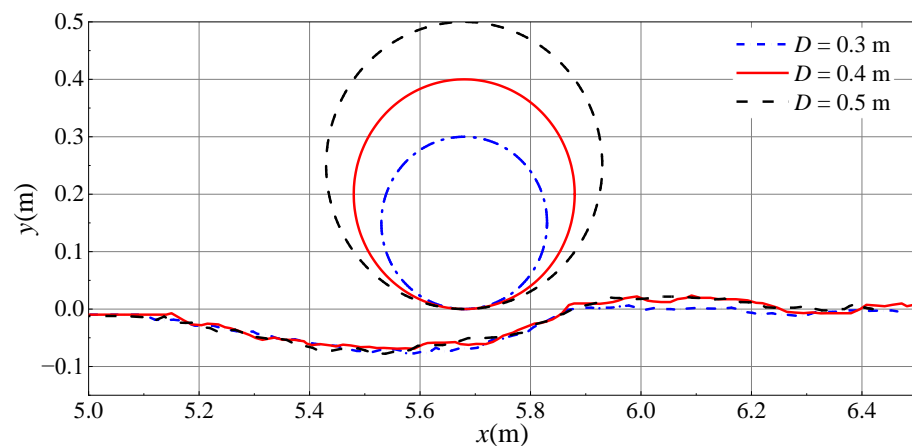


Figure 17. Bed profiles around the pipeline at $t = 10$ s for different pipeline diameters.

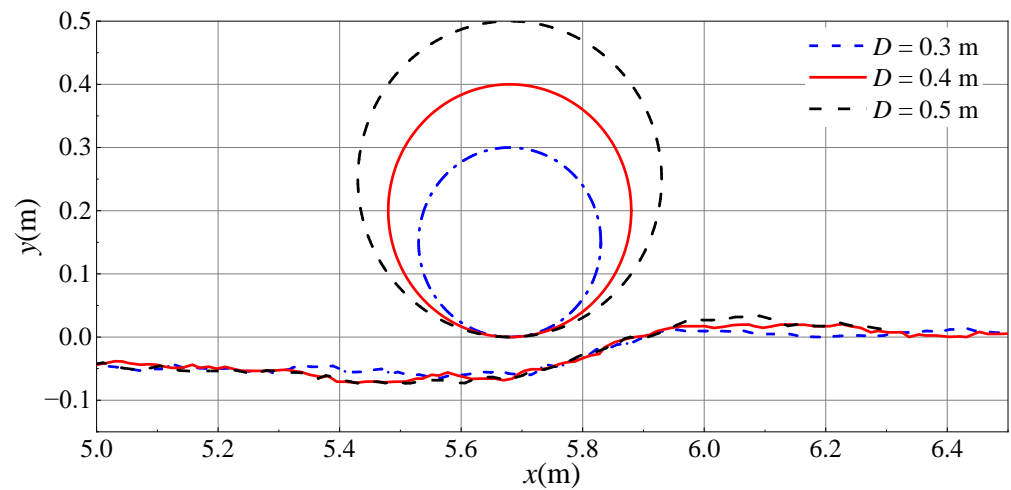


Figure 18. Bed profiles around the pipeline at $t = 15$ s for different pipeline diameters.

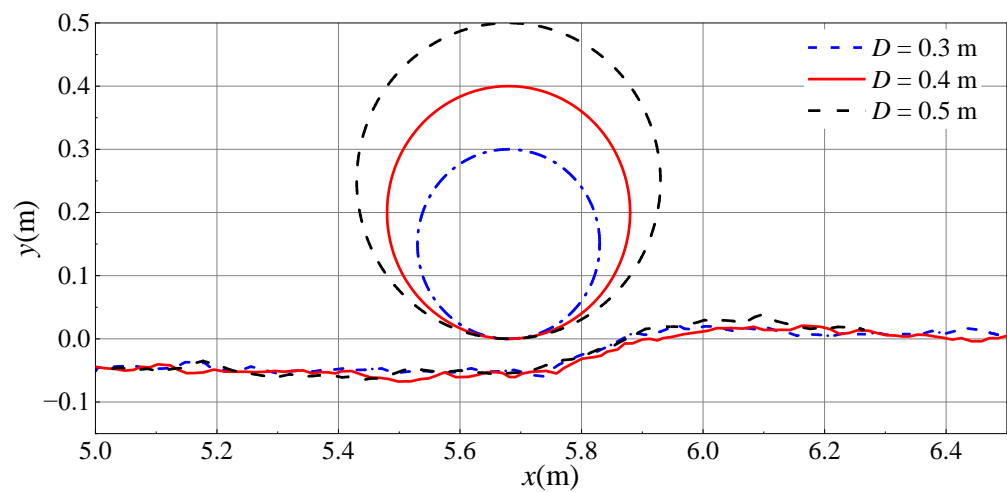


Figure 19. Bed profiles around the pipeline at $t = 20$ s for different pipeline diameters.

From the velocity contour maps of different diameters shown in Figure 20, it can be observed that as the pipeline diameter increases, the influence of the pipeline on the nearby flow field becomes more pronounced. The red area above the pipeline increases, indicating an increased flow velocity through the pipeline. Moreover, as the pipeline diameter increases, the flow velocity also increases.

As the pipeline diameter increases, the velocity decreases in the area behind the pipeline. A larger diameter creates a larger region of low velocity, resulting in slower flow. With the gradual increase in the gap below the pipeline, the velocity beneath the pipeline also increases. This increase in velocity, along with the widening of the gap between the pipeline and the bed surface, leads to deeper erosion and more sediment accumulation behind the pipeline.

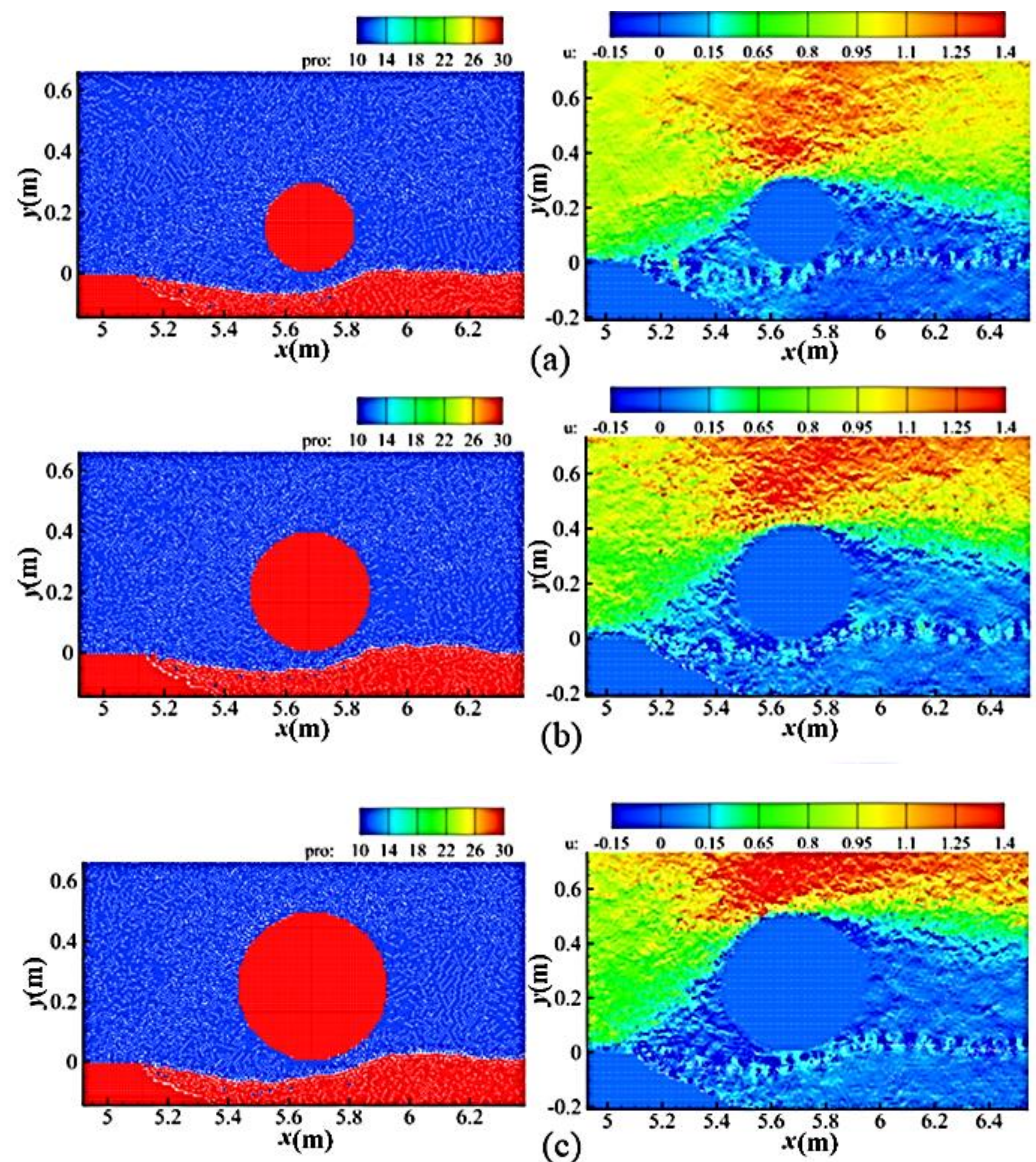


Figure 20. Bed profiles around the pipeline (left column) and velocity contour of the flow field (right column) for different pipeline diameters $D = 0.3$ m (a), 0.4 m (b), and 0.5 m (c).

In order to better understand the influence of different pipeline diameters on erosion morphology and maximum scour depth, curves depicting the variation in maximum scour depth with time were plotted under the same inflow velocity condition. Figure 21 shows that when the pipeline diameter is 0.3 m, the maximum scour depth (y/D) is the greatest, while it is the smallest when the diameter is 0.5 m. The erosion intensity also rapidly develops during the initial erosion stage, with a speed several times faster than that of the later erosion stage. Furthermore, a certain pattern emerges: as the pipeline diameter increases, the slope of the curve becomes smaller and the maximum scour depth reached decreases. After a certain period of erosion, the change in scour depth becomes minimal. Additionally, larger pipeline diameters result in smaller equilibrium scour depths.

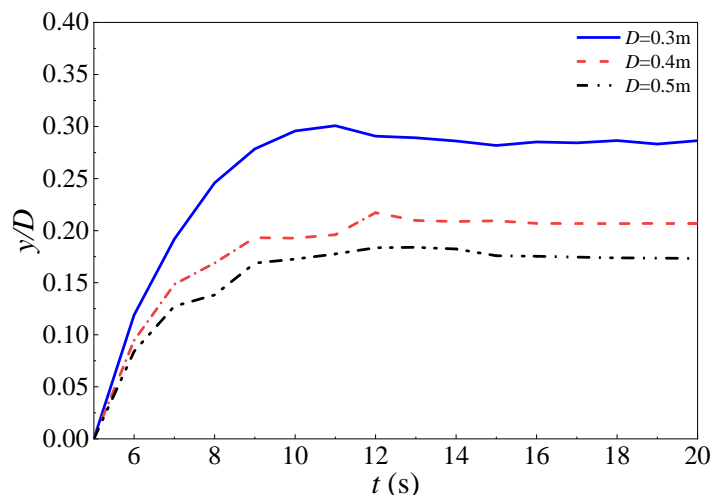


Figure 21. Maximum scour depth over time for different pipeline diameters.

4.4. The Equilibrium Time for Different Conditions

The time it takes for erosion to reach equilibrium under different conditions can provide insights into the development rate of erosion in engineering projects. When erosion reaches an equilibrium state, the scour depth no longer undergoes significant changes.

Figure 22a shows the scour equilibrium times for different gap ratios e/D . Under the condition of $e/D = 0$, the scour equilibrium time near the pipeline is the slowest, taking 11 s. On the other hand, under the condition of $e/D = 1.0$, the scour equilibrium time near the pipeline is the fastest, taking 9 s. As the gap ratio (e/D) increases, the scour equilibrium time gradually decreases.

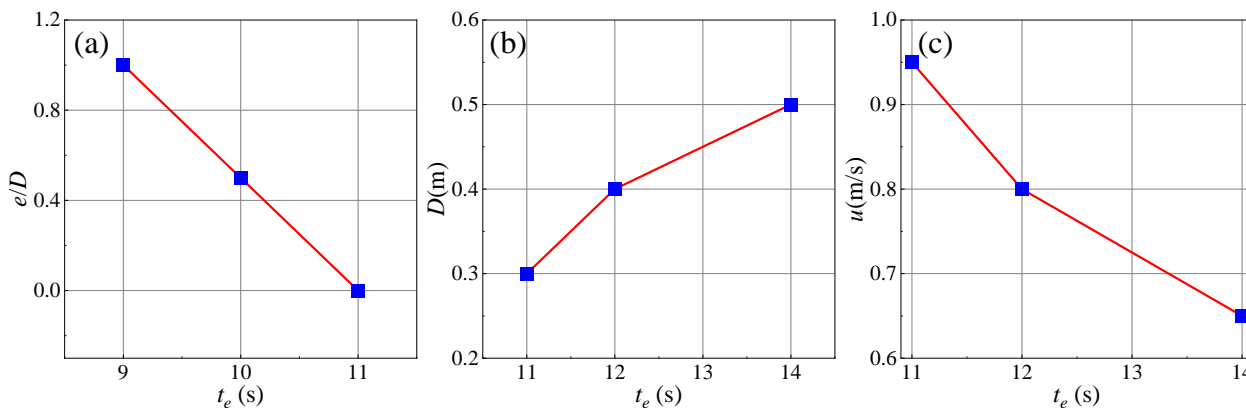


Figure 22. Scour equilibrium time t_e under different conditions. (a) different gap ratios; (b) different pipeline diameters; (c) different inlet flow velocities.

Figure 22b shows the scour equilibrium times for different pipeline diameters, D . Under the condition of $D = 0.5$ m, the scour equilibrium time near the pipeline is the slowest, taking 14 s. Conversely, under the condition of $D = 0.3$ m, the scour equilibrium time near the pipeline is the fastest, taking 11 s. As the pipeline diameter increases, the scour equilibrium time gradually decreases.

Figure 22c shows the curves of scour equilibrium times for different inlet flow velocities. The fastest scour equilibrium time is observed at an inlet flow velocity of $u = 0.95$ m/s, which takes 11 s. On the other hand, the slowest scour equilibrium time is observed at an inflow velocity of $u = 0.65$ m/s, which takes 14 s. As the inlet flow velocity increases, the time to reach scour equilibrium becomes shorter.

From the above analysis, it can be observed that a smaller gap ratio, lower inflow velocity, and larger pipeline diameter can all slow down the scour equilibrium time. This

provides a useful approach for protecting against sediment erosion near the pipeline in the future. If we can reduce the inflow velocity near the pipeline and bury the pipeline as deeply as possible into the seabed, it can greatly prevent the development of erosion, impede sediment transport, and avoid the formation of scour pits beneath the pipeline.

5. Discussion

The CWP-TWP-CSS erosion model shows promise in enhancing the accuracy of the ISPH method in simulating scour behind pipelines subjected to unidirectional steady flow. It effectively predicts both the ultimate scour depth and the shape of the scour pit. Compared to alternative methods, such as the critical velocity method, the CSS model demonstrates superiority in stability and accuracy in capturing scouring processes. Additionally, exploring the relationship between scouring depth and vortex size numerically could elaborate on the physical mechanisms underlying the relationships of relative scour depth under different conditions, i.e., pipeline diameters, gap ratios, and flow velocities. The faster erosion pace in numerical simulations compared to physical experiments is attributed to the size of numerical particles. Addressing this challenge would improve the model's predictive capabilities. In the future research, the $k-\varepsilon$ turbulence model will be incorporated and a three-dimensional local scour process around the pipelines will be simulated by the 3D ISPH two-phase flow model. Additionally, more complex seabed topographies, such as sand waves and other periodic undulating topographies [34,35], will be studied to understand their impact on sediment erosion around pipelines.

6. Conclusions

In this study, the ISPH method is modified to simulate the sediment erosion process around a two-dimensional submarine pipeline. The SPS turbulence model, sediment erosion model, and two-phase flow model are incorporated to investigate the local erosion phenomena around the submarine pipeline under the action of water flow. The characteristics of the flow field and vortex motion, and their impacts on the equilibrium scour depth are thoroughly explored under different conditions, including gap ratios ($e/D = -0.25, 0, 0.25, 0.5, 0.75, \text{ and } 1.0$), pipeline diameters ($D = 0.3 \text{ m}, 0.4 \text{ m}, \text{ and } 0.5 \text{ m}$), and inflow velocities ($u = 0.65 \text{ m/s}, 0.8 \text{ m/s}, \text{ and } 0.95 \text{ m/s}$). The main conclusions are summarized as follows:

- (1) The simulation results of the flow field and erosion model, obtained by establishing the simulation model for sediment erosion around the submarine pipeline and comparing these with experimental results, demonstrate that the ISPH method is applicable for studying sediment erosion around submarine pipelines.
- (2) When the pipeline diameter is $D = 0.3 \text{ m}$ and the inflow velocity is $u = 0.95 \text{ m/s}$, the maximum scour depth initially increases and then decreases with the increase in the gap ratio e/D . The maximum scour depth is achieved when $e/D = 0.5$. When the pipeline diameter is $D = 0.3 \text{ m}$ and the gap ratio is 0, the maximum scour depth increases with the increase in the inflow velocity. The maximum scour depth is achieved when $u = 0.95 \text{ m/s}$. When the inflow velocity is $u = 0.95 \text{ m/s}$ and the gap ratio is 0, the maximum scour depth gradually decreases with the increase in the pipeline diameter. The minimum maximum scour depth is achieved when $D = 0.5 \text{ m}$.

Author Contributions: Conceptualization, S.Y. and D.W.; methodology, D.W.; software, D.W.; validation, D.W., Y.G. and S.Y.; formal analysis, Y.G.; investigation, Y.G. and S.Y.; resources, D.W.; data curation, D.W.; writing—original draft preparation, D.W. and Y.G.; writing—review and editing, S.Y., D.W., Y.L., J.L. and Y.S.; visualization, Y.G.; supervision, D.W.; project administration, D.W.; funding acquisition, D.W. and Y.L. All authors have read and agreed to the published version of the manuscript.

Funding: This work was supported by the National Natural Science Foundation of China (Grant number 52101299, 52301320); the Open Fund of Fujian Province Key Laboratory of Ship and Ocean Engineering; Fundamental Research Funds for the Central Universities of China (Grant number

3132023360 and 3132023167); the Open Fund of State Key Laboratory of Hydraulic Engineering Intelligent Construction and Operation (Grant number HESS-2113), and Natural Science Funds of Fujian Province (Grant number 2023J01790).

Data Availability Statement: The authors confirm that the data supporting the findings of this study are available from the corresponding author upon reasonable request.

Conflicts of Interest: The authors declare no conflicts of interest.

References

- Chiew, Y. Mechanics of Local Scour around Submarine Pipelines. *J. Hydraul. Eng.* **1990**, *116*, 515–529. [[CrossRef](#)]
- Chiew, Y. Prediction of Maximum Scour Depth at Submarine Pipelines. *J. Hydraul. Eng.* **1991**, *117*, 452–466. [[CrossRef](#)]
- Lee, C.H.; Low, Y.M.; Chiew, Y.M. Multi-dimensional rheology-based two-phase model for sediment transport and applications to sheet flow and pipeline scour. *Phys. Fluids* **2016**, *28*, 053305.
- Fredsøe, J. Pipeline–seabed interaction. *J. Waterw. Port Coast.* **2016**, *142*, 03116002. [[CrossRef](#)]
- Ahmad, N.; Bihs, H.; Myrhaug, D.; Kamath, A.; Arntsen, Ø.A. Numerical modelling of pipeline scour under the combined action of waves and current with free-surface capturing. *Coast. Eng.* **2019**, *148*, 19–35. [[CrossRef](#)]
- Zhao, M. A review on recent development of numerical modelling of local scour around hydraulic and marine structures. *J. Mar. Sci. Eng.* **2022**, *10*, 1139. [[CrossRef](#)]
- Dey, S.; Singh, N.P. Clear-Water Scour below Underwater Pipelines under Steady Flow. *J. Hydraul. Eng.* **2008**, *134*, 588–600. [[CrossRef](#)]
- Cheng, L.; Yeow, K.; Zhang, Z. Three-dimensional scour below offshore pipelines in steady currents. *Coast. Eng.* **2009**, *56*, 577–590. [[CrossRef](#)]
- Sumer, B.M.; Truelsen, C.; Sichmann, T.; Fredsøe, J. Onset of scour below pipelines and self-burial. *Coast. Eng.* **2001**, *42*, 313–335. [[CrossRef](#)]
- Sumer, B.M.; Jensen, H.R.; Mao, Y. Effect of Lee-Wake on Scour Below Pipelines in Current. *J. Waterw. Port Coast.* **1988**, *114*, 599–614. [[CrossRef](#)]
- Li, F.; Cheng, L. Numerical model for local scour under offshore pipelines. *J. Hydraul. Eng.* **1999**, *125*, 400–406. [[CrossRef](#)]
- Liang, D.; Cheng, L.; Li, F. Numerical modeling of flow and scour below a pipeline in currents. Part II. Scour simulation. *Coast. Eng.* **2005**, *52*, 43–62. [[CrossRef](#)]
- Liang, D.; Cheng, L.; Yeow, K. Numerical study of the Reynolds-number dependence of two-dimensional scour beneath offshore pipelines in steady currents. *Ocean Eng.* **2005**, *32*, 1590–1607. [[CrossRef](#)]
- Zhao, M.; Cheng, L. Numerical modeling of local scour below a piggyback pipeline in currents. In Proceedings of the International Conference on Offshore Mechanics and Arctic Engineering—OMAE, Hamburg, Germany, 4–9 June 2006; pp. 1452–1463.
- Yeganeh-Bakhtiary, A.; Kazeminezhad, M.H.; Etemad-Stemad-Shahidi, A. Euler-Euler two-phase flow simulation of tunnel erosion beneath marine pipelines. *Appl. Ocean Res.* **2011**, *33*, 137–146. [[CrossRef](#)]
- Khayyer, A.; Gotoh, H.; Shao, S.D. Corrected Incompressible SPH method for accurate water-surface tracking in breaking waves. *Coast. Eng.* **2008**, *55*, 236–250. [[CrossRef](#)]
- Wang, D.; Li, S.; Arikawa, T.; Gen, H. ISPH simulation of scour behind seawall due to continuous tsunami overflow. *Coast. Eng. J.* **2016**, *58*, 1650014. [[CrossRef](#)]
- Fonty, T.; Ferrand, M.; Leroy, A.; Joly, A.; Violeau, D. Mixture model for two-phase flows with high density ratios: A conservative and realizable SPH formulation. *Int. J. Multiph. Flow.* **2019**, *111*, 158–174. [[CrossRef](#)]
- Bertevas, E.; Tran-Duc, T.; Le-Cao, K.; Khoo, B.C.; Phan-Thien, N. A smoothed particle hydrodynamics (SPH) formulation of a two-phase mixture model and its application to turbulent sediment transport. *Phys. Fluids* **2019**, *31*, 103–303. [[CrossRef](#)]
- Akbari, H.; Pooyarad, A. Wave force on protected submarine pipelines over porous and impermeable beds using SPH numerical model. *Appl. Ocean Res.* **2020**, *98*, 102118. [[CrossRef](#)]
- Mirmohammadi, A.; Ketabdari, M.J. Numerical simulation of wave scouring beneath marine pipeline using smoothed particle hydrodynamics. *Int. J. Sediment Res.* **2011**, *26*, 331–342. [[CrossRef](#)]
- Zanganeh, M.; Yeganeh-Bakhtiary, A.; Abd Wahab, A.K. Lagrangian coupling two-phase flow model to simulate current-induced scour beneath marine pipelines. *Appl. Ocean Res.* **2012**, *38*, 64–73. [[CrossRef](#)]
- Wang, D.; Shao, S.; Li, S. 3D ISPH erosion model for flow passing a vertical cylinder. *J. Fluids Struct.* **2018**, *78*, 374–399. [[CrossRef](#)]
- Gotoh, H.; Shibahara, T.; Sakai, T. Sub-Particle-Scale Turbulence Model for the MPS Method Lagrangian Flow Model for Hydraulic Engineering. *Comput. Fluid Dyn. J.* **2001**, *9*, 339–347.
- Smagorinsky, J. General circulation experiments with the primitive equations: I. The basic experiment. *Mon. Weath. Rev.* **1963**, *91*, 99–164. [[CrossRef](#)]
- Chorin, A.J.; Marsden, J.E. *A Mathematical Introduction to Fluid Mechanics*; Texts in Applied Mathematics; Springer: New York, NY, USA, 1990.
- Monaghan, J.J. Smoothed particle hydrodynamics. *Annu. Rev. Astron. Astrophys.* **1992**, *30*, 543–574. [[CrossRef](#)]
- Khayyer, A.; Gotoh, H. A higher order Laplacian model for enhancement and stabilization of pressure calculation by the MPS method. *Appl. Ocean Res.* **2010**, *32*, 124–131. [[CrossRef](#)]

29. Schlichting, H. *Boundary Layer Theory*, 7th ed.; McGraw-Hill Book Co.: New York, NY, USA, 1987.
30. Manenti, S.; Sibilla, S.; Gallati, M.; Agate, G.; Guandalini, R. SPH simulation of sediment flushing induced by a rapid water flow. *J. Hydraul. Eng.* **2012**, *138*, 272–284. [[CrossRef](#)]
31. Zhang, R.J.; Xie, J.H.; Chen, W.B. *River Dynamics*; Wuhan University Press: Wuhan, China, 2007.
32. Oner, A.A.; Kirkgoz, M.S.; Akoz, M.S. Interaction of a current with a circular cylinder near a rigid bed. *Ocean Eng.* **2008**, *35*, 1492–1504. [[CrossRef](#)]
33. Akter-Uz-Zaman, M. Two-Dimensional Local Scour Numerical Simulation of Submarine Pipeline Based on Two-Phase Flow Model. Ph.D. Thesis, Tianjin University, Tianjin, China, 2020.
34. Gao, J.; Hou, L.; Liu, Y.; Shi, H. Influences of bragg reflection on harbor resonance triggered by irregular wave groups. *Ocean Eng.* **2024**, *305*, 117941. [[CrossRef](#)]
35. Gao, J.; Shi, H.; Zang, J.; Liu, Y. Mechanism analysis on the mitigation of harbor resonance by periodic undulating topography. *Ocean Eng.* **2023**, *281*, 114923. [[CrossRef](#)]

Disclaimer/Publisher’s Note: The statements, opinions and data contained in all publications are solely those of the individual author(s) and contributor(s) and not of MDPI and/or the editor(s). MDPI and/or the editor(s) disclaim responsibility for any injury to people or property resulting from any ideas, methods, instructions or products referred to in the content.